Destabilization of a planar liquid stream by a co-flowing turbulent gas stream

Delin Jiang, Yue Ling*

Department of Mechanical Engineering, Baylor University, Waco, Texas 76798, United States

Abstract

In Airblast atomization, the disintegration of a liquid stream is assisted by a co-flowing high speed gas stream. The shear instability develops at the interface, forming interfacial waves that propagate and eventually break into droplets downstream. In the present study, the destabilization of a planar liquid stream by a co-flowing gas stream with different turbulence intensities is investigated through direct numerical simulation. A parametric study is conducted to investigate the effect of gas inlet turbulence intensity on the interfacial instability near the nozzle exit and the development of two-phase mixing layer downstream. The gas-liquid interface is resolved by a momentum-conserving volume-of-fluid method. A digital filter approach is used to generate temporally and spatially correlated turbulent velocity fluctuations at the gas inlet. The interfacial stability is absolute for all cases considered. The dominant frequency and the spatial growth rate corresponding to the most unstable mode are measured and compared with experiments and spatial-temporal linear stability analysis. The numerical results of the dom-

*Corresponding author. Address: One Bear Place #97356, Waco, TX 76798
Email address: staney_ling@baylor.edu (Yue Ling)

inant frequencies agree well with the experimental data. Both the dominant frequency and the spatial growth rate increase with the gas inlet turbulence intensity, after passing a threshold value. The linear stability analysis with the turbulent eddy viscosity model captures the increasing trends of the dominant frequency and the spatial growth rate but significantly underpredicts the values. Two-phase turbulence statistics, including Reynolds stresses and turbulent kinetic energy dissipation, are also presented. It is shown that the gas inlet turbulence tends to enhance interaction between the two streams near the nozzle exit and to reduce the interaction downstream.
Keywords: Airblast atomization, DNS, Interfacial instability, Two-phase turbulence

1. Introduction

When two parallel streams of gas and liquid with different velocities meet, the shear between the two streams triggers an instability at the interface separating the gas and liquid. The shear instability induces wavy coherent structures, and these interfacial waves grow, roll up and eventually break into droplets. The droplets are dispersed by the turbulent gas stream, forming a turbulent two-phase mixing layer. The destabilization of bulk liquids assisted by a co-flowing gas stream is essential to liquid fuel injections through airblast atomizers, which are commonly seen in aerospace engines [1].

Shear-induced interfacial instability is a classic fundamental problem in fluid dynamics. The earliest work can be traced back to the inviscid temporal stability theory (known as the Kelvin-Helmholtz instability) in the 19th century [2, 3]. Since then, the inviscid stability analysis has been studied

by many others, see for example [4, 5, 6, 7]. The stability analysis was extended to incorporate the viscous effect (namely the Orr-Sommerfeld theory) [8, 9, 10] and to account for the instability induced by the viscosity contrast across the interface [11]. Though temporal analyses have been extensively used, to better represent shear interfacial instability in realistic atomization processes, recent studies have moved toward spatio-temporal analyses [12, 13, 14]. The interfacial instability can be convective or absolute depending on injection conditions (such as injection velocities) and the fluid properties (such as density, viscosity, and surface tension) [13, 15, 14]. For an absolute instability, a dominant frequency arises and the formation of interfacial waves near the nozzle has been observed to be dictated by the most-unstable mode [6, 16, 17].

When the two streams are both laminar, the capability of the linear stability theory (spatio-temporal viscous analysis) in predicting the most-unstable frequency has been confirmed by both experiments [16, 14] and direct numerical simulations (DNS) [17, 18]. However, when the inlet gas stream is turbulent, theoretical prediction of the most-unstable mode remains to be established. It has been observed in experiments that the dominant frequency increases significantly with the intensity of turbulent velocity fluctuations at the gas inlet. Former studies have been made to account for the effect of gas turbulence on interfacial stability by using the eddy-viscosity model in viscous stability analysis [15]. However, when this technique is applied to the present problem of airblast atomization, the theoretical predictions significantly underestimated the dominant frequency, see [14] and also our results to be shown later. The underlying mechanisms that cause the increase of

dominant frequency due to inlet gas turbulence is still not fully understood. The impact of the inlet gas turbulence on the interfacial wave breakup and the two-phase mixing layer downstream remains to be explored.

In the present study, we perform direct numerical simulations of air-blast atomization with turbulent fluctuations of different intensity magnitudes present at the gas inlet. Through the high-fidelity simulation results, we aim to address following key questions:

- How does the inlet gas turbulence influence the interfacial instability, including the dominant frequency and spatial growth rate?
- How does the modulated interfacial instability in turn influence the development of the two-phase mixing layer?

Improving the Orr-Sommerfeld theory by incorporating the effect of inlet gas turbulence is of interest, since it can provide predictions of important features such as the dominant frequency and growth rate with much lower costs compared to full simulation. Though extending stability theory or two-phase turbulence modeling are out of the scope of the present work, the simulation results provided in the present study will be critical to future investigation on that subject.

2. Simulation Methods

2.1. Simulation Setup

The simulation setup is shown in Fig. 1, which is similar to our previous works [19, 18]. The domain is a rectangular box filled with stationary gas at $t = 0$. Then the two parallel planar gas and liquid streams enter the domain

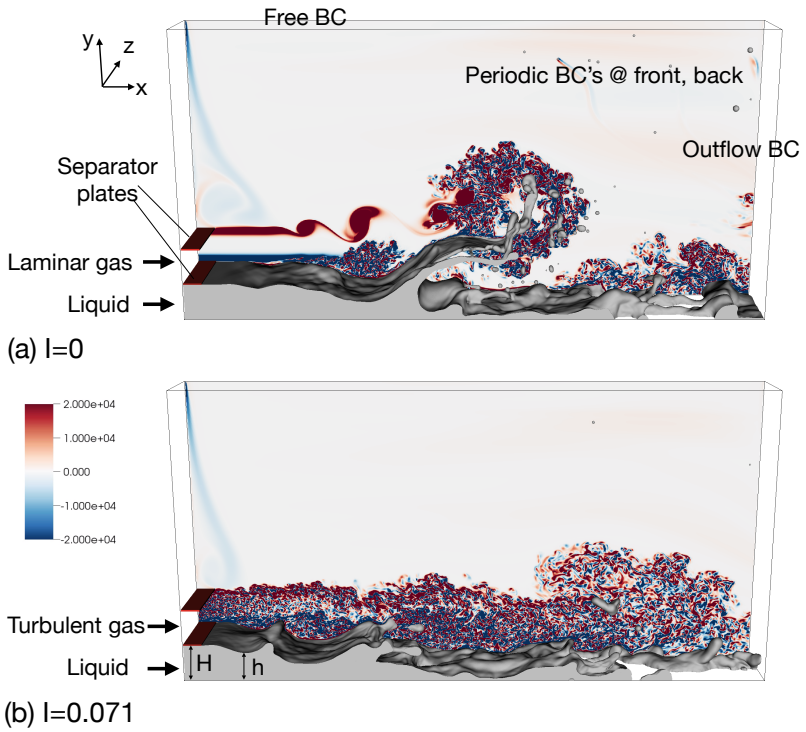

Figure 1: Two-phase mixing layers with (a) a laminar inlet gas stream ($I = 0$) and (b) a turbulent gas inlet stream ($I = 0.071$). The background is the z-vorticity.

from the left. The liquid inflow is laminar, while the gas inflow can be laminar or turbulent, which can be identified through the z-vorticity plotted in the background. When the gas inflow is turbulent, different magnitudes of turbulence intensity, I, are considered. The turbulence intensity I here represents the root mean square of velocity fluctuations normalized by the mean velocity at the nozzle exit. Two separator plates are introduced to mimic the effect of injector nozzle, separating the liquid and gas streams and the injected gas and the stationary gas originally in the domain. The dimensions of the two separator plates are identical: the thickness is $\eta = H/32$ and the length is $\beta = H/2$. Based on former studies, the plate thickness here is small enough and has little effect on the interfacial instability [16]. The thickness of the vorticity layers at the gas and liquid inlets are both $\delta = H/8$, respectively. The height of the inlet gas stream is $H - \eta$ and that of the liquid stream is H. The length, height, and width of the computational domain are $16H$, $8H$, and $2H$, respectively.

The mean flow at the inlet is horizontal ($\overline{v}_0 = \overline{w}_0 = 0$) and the streamwise component of velocity is specified as

$$\overline{u}_{in}(y) = \begin{cases} U_l \operatorname{erf}\left[\frac{H-y}{\delta_g}\right], & 0 \le y < H, \\ 0, & H \le y < H+\eta, \\ U_g \operatorname{erf}\left[\frac{y-(H+\eta)}{\delta_g}\right] \operatorname{erf}\left[\frac{2H-y}{\delta_g}\right], & H+\eta \le y < 2H, \\ 0, & \text{else}, \end{cases} \tag{1}$$

where U_l and U_g are the liquid and gas injection velocities and δ_g is the vorticity layer thickness for the mean flow. The values of these parameters are given in table 1.

Since the mean flow is two dimensional (x-y), averaging is conducted

spatially in the z direction and also in time. The averaging operator $\overline{()}$ is defined as

$$\overline{u}(x,y) \equiv \frac{1}{t_1 - t_0}\frac{1}{L_z}\int_{t_0}^{t_1}\int_0^{L_z} u(x,y,z,t)\, dz\, dt\,, \tag{2}$$

where t_0 and t_1 are the starting and ending sampling times, assuming the two-phase mixing layer has reached the statistically steady state at t_0. The fluctuation away from the mean quantity is denoted by $u' = u - \overline{u}$.

The total velocity imposed at the gas inlet ($H + \eta \leq y < 2H$) is

$$u_{in} = \overline{u}_{in} + u'(y,z,t)\,, \quad v_{in} = v'(y,z,t)\,, \quad w_{in} = w'(y,z,t)\,, \tag{3}$$

The digital filter approach of Klein *et al.*[20] is employed to generate temporally and spatially correlated velocity fluctuations, u', v', w' (corresponding to subscript $i = 1, 2, 3$ respectively), at the gas inlet:

$$u_i' = a_{ij}\mathcal{U}_j\,, \tag{4}$$

where $\mathcal{U}_j$ is the filtered random fluctuations and a_{ij} is the transformation tensor.

Given a series of random data r_j with $\overline{r_j} = 0$ and $\overline{r_j r_j} = 1$, then the random data is filtered as

$$\mathcal{U}_j = \sum_{n=-N}^{N} b_n r_{j+n}\,, \tag{5}$$

where b_n are the filter coefficients and a Gaussian filter is used here.

The transformation tensor a_{ij} is given as

$$a_{ij} = \begin{bmatrix} (R_{11})^{1/2} & 0 & 0 \\ R_{21}/a_{11} & (R_{22} - a_{21}^2)^{1/2} & 0 \\ R_{31}/a_{11} & (R_{32} - a_{21}a_{31})/a_{22} & (R_{33} - a_{31}^2 - a_{32}^2)^{1/2} \end{bmatrix},$$

where R_{ij} is the correlation tensor, and we approximate that the diagonal terms of R_{ij} are identical to $I^* U_g$ and the off-diagonal terms are equal to zero, where I^* is the normalized intensity of velocity fluctuations at the gas inlet, namely

$$\sqrt{\overline{u'u'}}/U_g = \sqrt{\overline{v'v'}}/U_g = \sqrt{\overline{w'w'}}/U_g = I^* \,. \tag{6}$$

This simplification assumes the turbulence at the gas inlet is homogeneous. As gas flows between the two separator plates, boundary layers develops and turbulence homogeneity will vanish and when gas and liquid meet at the nozzle exit, the gas turbulence is non-homogeneous, as can be observed in Figs. 2(b) and (c).

The length and time scales of the turbulence generated, $\mathcal{L}$ and $\mathcal{T}$, are controlled by the spatial and temporal width of the filter. In the present study, the width of the Gaussian filter is $\mathcal{L} = H/16$ and the time scale is $\mathcal{T} = \mathcal{L}/U_g$, based on the Taylor Hypothesis. The frequency of the inlet gas turbulence is at least two orders of magnitudes higher than the dominant frequency of the interfacial instability. Therefore, the increase of most-unstable frequency at the gas-liquid interface when turbulence is present at the gas inlet is due the turbulence-enhanced coupling between the gas and liquid streams, and is not sensitive to the length and time scales of the gas inlet turbulence. The turbulence intensity at the gas inlet (I^*) is the key parameter to characterize the effect on the inlet gas turbulence on the destabilization of the liquid layer.

To systematically investigate the effect of the inlet gas turbulence intensity, five different values of I^* are considered. The profiles of the mean velocity and covariance of the velocity fluctuations, $\overline{u'u'}$ and $\overline{u'v'}$, near the in-

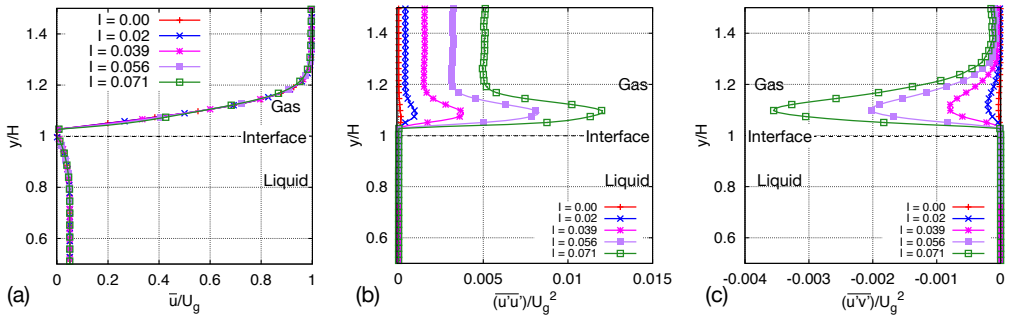

Figure 2: Profiles of (a) the mean velocity (b) the normal Reynolds stress $\overline{u'u'}$ and (c) the shear Reynolds stress $\overline{u'v'}$ at the nozzle exit $x = \beta$.

terface ($0.5 < y/H < 1.5$) at the nozzle exit ($x = \beta$) are shown in Fig. 2. Due to the no-slip condition at the separator plate, a wake is formed downstream of the plate, introducing a velocity deficit in the mean streamwise-velocity profiles. The mean velocity profiles for all cases are very similar, while the magnitudes of the velocity fluctuation covariances increase with I^*. When $I^* = 0$ then inlet gas stream is laminar, and the case is similar to our previous simulations [19, 18]. The values of $\overline{u'u'}$ for different I^* in the middle of the gas stream ($y > 1.2H$) are nearly constant, the square root of which is denoted by $I = \sqrt{\overline{u'u'}}|_{nozzle-exit}/U_g$. Instead of I^*, we use I to characterize the turbulence intensity of the gas inlet since I is measured at the nozzle exit where the two streams meet. This choice is also consistent with the former experimental study [21] so that a direct comparison with the experimental data can be made. As indicated in Fig. 2(b), $I = 0$, 0.020, 0.039, 0.056, and 0.071 for $I^* = 0$, 0.05, 0.1, 0.15, 0.2, respectively.

The bottom surface the domain is set as a slip wall. As a simplified model of typical airblast atomizers, where gases are injected on both the top and the bottom of the liquid layer, the present simulation only considers half

of the domain. The slip-wall (symmetric) boundary will not influence the major conclusion regarding interfacial instability near the nozzle, since when the wave amplitude is much smaller than the thickness liquid layer thickness, the effect from the bottom boundary is negligible. Nevertheless, the bottom boundary will affect the instability of the liquid layer further downstream when the wave amplitude becomes large and comparable to the liquid layer thickness. To fully characterize the instability and breakup of the liquid layer, a simulation with the full domain will be required, which is relegated to our future work.

Periodic boundary conditions are applied to the domain surfaces in z-direction (front and back). A free boundary condition is invoked at the top where gas is allowed to freely enter or leave the boundary. The outflow boundary condition is imposed at the right surface. Discussions on the effects of the domain size and boundary conditions on the two-phase mixing layer development can be found in our former work [18].

The physical parameters are given in Table 1. The liquid phase is water, and the gas phase is a pressurized gas. Instead of using the exact parameters in experiments [21], we have chosen a case of moderate density ratio which has been extensively verified and validated [19, 18]. The key dimensionless parameters are listed in Table 2. For the gas-to-liqid dynamic pressure ratio $M = 20$ used here, the interfacial instability is expected to be absolute [16]. Due to the high Reynolds number for the gas stream, $\mathrm{Re}_{g,H}$, the gas stream will become turbulent even if it is laminar at the inlet.

To focus computational resources on the effect of inlet gas turbulence, the liquid-to-gas density ratio r and the gas Weber number We_g are fixed

in the present study. Nevertheless, these two parameters are important to the development of a two phase mixing layer. Zandian *et al.*[22, 23] identified different breakup mechanisms for a planar liquid jet for different Weber and Reynolds numbers. For low Weber numbers, liquid sheets formed wave crests breaks by forming fingers at the rim; while for large We_l, holes are formed in middle of liquid sheet and the expansion of holes eventually leads to the disintegration of liquid sheets. They also showed that density ratio affects the transitional boundaries between different breakup regimes. Former spatial-temporal stability analysis [13] and numerical simulations [16] have also shown that the critical dynamic-pressure ratio for convective/absolute instability transition generally increases with We_g and decreases with r. It is also shown that both We_g and r can influence the most unstable wave number and spatial growth rate [13]. In the present case, we have observed both fingering-induced and holes-induced breakups of sheets in our simulations. The conclusions made are only strictly valid for the moderate Weber number and density ratio used here and parametric studies for We_g and r are required in the future for a fully verification.

ρ_l	ρ_g	μ_l	μ_g	σ	U_l	U_g	H	δ_g
(kg/m^3)	(kg/m^3)	(Pa s)	(Pa s)	(N/m)	(m/s)	(m/s)	(mm)	(mm)
1000	50	10^{-3}	5×10^{-5}	0.05	0.5	10	0.8	0.1

Table 1: Physical parameters.

2.2. Numerical methods

We solve the Navier-Stokes equations for incompressible flow with sharp interfaces and constant surface tension with the open-source solver, *PARIS-*

M	r	m	$\mathrm{Re}_{g,\delta}$	$\mathrm{We}_{g,\delta}$	$\mathrm{Re}_{g,H}$	I
$\rho_g U_g^2/(\rho_l U_l^2)$	ρ_l/ρ_g	μ_l/μ_g	$\rho_g U_g \delta_g/\mu_g$	$\rho_g U_g^2 \delta_g/\sigma$	$\rho_g U_g H_g/\mu_g$	$\sqrt{\overline{u'u'}}\vert_{nozzle-exit}/U_g$
20	20	20	1000	10	7750	0 to 0.071

Table 2: Key dimensionless parameters.

Simulator. The interface is tracked using a momentum-conserving piecewise-linear geometric volume-of-fluid (VOF) method, where the advection of momentum near the interface is implemented in a manner consistent with the VOF advection [24]. The viscous term is treated explicitly with a second-order centered difference scheme. Curvature is computed using the height-function method, and the surface tension is calculated with the balanced continuous-surface-force method [25]. The fields are discretized using a fixed regular cubic grid with a cell size $\Delta = 6.25$ μm. The cell size has been shown to be adequate to yield good estimates of high-order two-phase turbulence statistics, such as TKE dissipation [18]. The total number of cells is about 0.5 billion. Calculations were performed with 1024 cores (Intel Xeon Platinum 8160). The total computational cost for all the cases presented is about 2 million core-hours in total.

3. Results and Discussion

3.1. General behavior

A qualitative comparison between the two cases with laminar ($I = 0$) and turbulent ($I = 0.071$) gas inlets is shown in Fig. 1. The liquid is colored in grey, and the background is the z-component of vorticity. The vorticity layer in blue color near the left boundary are induced by the gas entrained from

the top free boundary. When the inlet gas stream is laminar, two vorticity layers on the top and bottom of gas stream can be clearly seen. Both the gas-liquid interface and the gas-gas interface (separating the injected gas and that originally in the domain) are unstable, and the instabilities at these two interfaces develop gradually. The gas-gas interface does not form a roll-up vortex until about $2H$ downstream of the nozzle exit. The instability at the gas-liquid interface grows faster than the gas-gas interface, forming coherent wavy structures on the interface. The interfacial wave amplitude is initially small near the nozzle and grows as the wave is advected downstream. In the snapshot shown here, the height of the interfacial wave near the center of the domain is comparable or even larger than the gas stream thickness at the inlet (H), resulting in a strong interaction with the gas stream. A long liquid sheet is formed at the crest of the wave. The liquid sheet flaps, and holes are formed in it. Eventually the holes expand, fragmenting the liquid sheet into multiple ligaments and droplets, accompanied with the generation of many small vortices. Discussions about the drop formation mechanisms in airblast atomization can be found in our former work [19].

On the other hand, when turbulence is present at the gas inlet, the vorticity layers at the gas-gas and gas-liquid interfaces near the nozzle exit become irregular and are distorted by the inlet turbulence. Similar interfacial distortion can also be observed in [26] near the nozzle. The shear due to the mean flow velocity differences (between the injected gas and liquid streams and between the injected gas and the stationary gas) can still be recognized from the darker red and blue colors near the gas-gas and gas-liquid interfaces. Furthermore, the instability at the gas-liquid interface develops faster

compared to that for the laminar gas inlet. The amplitude of the interfacial wave near the nozzle (such as at a distance H downstream of the nozzle exit) is significantly larger for $I = 0.071$ than that for $I = 0$. In the snapshot in Fig. 1(b) two waves are observed, while only one can be recognized for the case with a laminar gas inlet shown in Fig. 1(a). This seems to indicate that the wavelength is reduced due to the addition of inlet gas turbulence. In contrast to the increase of wave amplitude near the nozzle, the wave amplitude downstream for $I = 0.071$ is reduced. No sheet flapping nor violent sheet fragmentation are observed for $I = 0.071$.

At the interface between turbulent gas and nonturbulent ambient gas, the laminar gas is entrained into the turbulent gas stream through small-scale eddying at the interface [27]. However, at the gas-liquid interface that separates the turbulent gas and laminar liquid, the laminar liquid can only be entrained into the turbulent gas stream as interfacial waves with length scales much larger than the turbulent vortices. A "strictly" speaking mixing does not happen until the liquid sheet breaks and form a turbulent dispersion of small droplets. Since the focus of the present study is on the gas-liquid interface and the physics related to the gas-gas interface is of secondary importance, from here on we simply refer to "interface" as the gas-liquid interface, unless otherwise stated.

3.2. Dominant frequency

The wave propagation speed, U_w, is measured from the simulation results, and it is found that U_w changes little with the inlet gas turbulence intensity I. The wave speed (averaged over the multiple waves covered in the simulation duration) is about $U_w = 0.22U_g$, which agrees well with the prediction given

by the Dimotakis theory [28], *i.e.*,

$$U_w = \frac{\sqrt{\rho_l}U_l + \sqrt{\rho_g}U_g}{\sqrt{\rho_l} + \sqrt{\rho_g}}\,. \tag{7}$$

The agreement between wave speed for different I with Dimotakis speed has also been observed in experiments [21]. Since the wavelength can be related to the wave speed and formation frequency as $f_0 = U_w/l_w$, the shorter wavelength l_w observed in Fig. 1 for $I = 0.071$ is indeed an outcome of the increased frequency.

The temporal evolution of the interfacial height h near the nozzle (measured at $x/H = 0.625$) for $I = 0$ and 0.071 are shown in Fig. 3(a). The interfacial height h is measured from the interface to the bottom of the domain along the y direction, see Fig. 1. The value of h shown here is averaged over the z direction, though the variation of h over z near the nozzle is quite small. For both cases of $I = 0$ and 0.071, h oscillates in time. When turbulent fluctuations are present at the gas inlet ($I = 0.071$), the oscillation amplitude is significantly larger, and the oscillation period is reduced. The frequency spectra, obtained by Fourier transform of the temporal variation of h, are shown in Fig. 3(b). The dominant frequencies, denoted as f_0, for the two cases are clearly different (indicated by the vertical dotted lines). When I increases from 0 to 0.071, the dominant frequency shifts to the right from $f_0 H/U_g = 0.050$ and 0.079.

Figure 3(c) shows the numerical results for f_0 as a function I, compared to the experimental data of Matas *et al.*[14]. Both of the numerical and experimental results show that f_0 increases with I. In the experiment, the data for a wide range of injection conditions (different combinations of U_g and U_l are denoted by different symbols) are shown to be constrained in a region

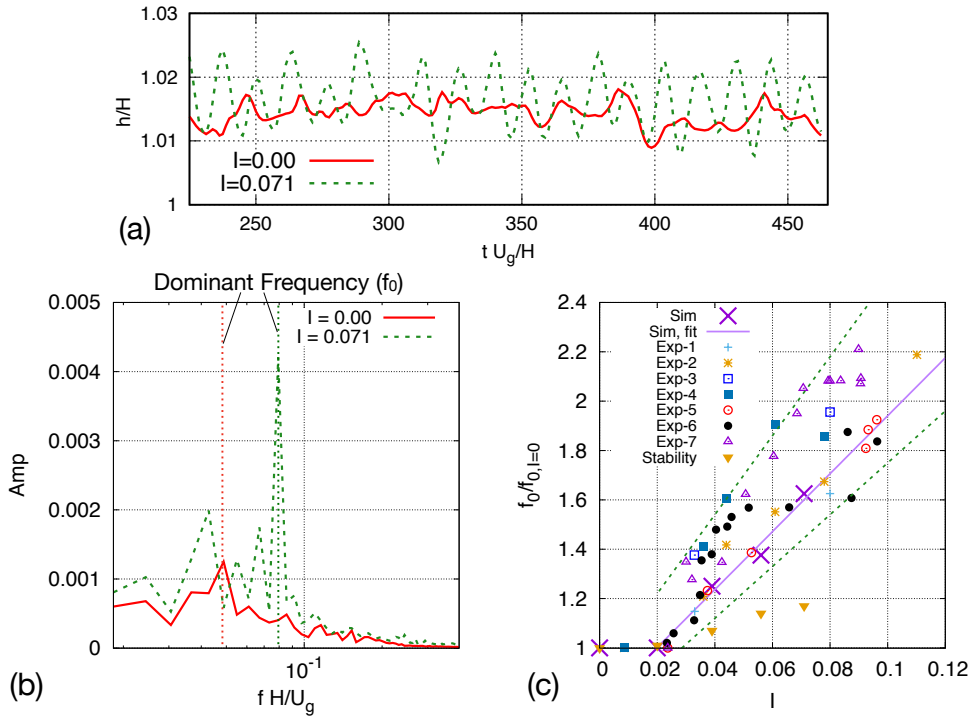

Figure 3: (a) Temporal evolutions and (b) spectra of the interface height h at $x/H = 0.625$. (c) Variation of the dominant frequency with the inlet gas turbulence intensity I for the present simulation and the experiment of [21] (different symbols denote different injection conditions).

bounded by the two dotted lines ($f_0/f_{0,I=0} = 10.5I + 0.7$ and $f_0/f_{0,I=0} = 16I + 0.9$). The variation of f_0 with I for the present simulation results are within this region and in general agree well with the experimental data.

Though dominant frequency generally increases with I, the numerical results show that $f_0/f_{0,I=0}$ varies little for $I < 0.02$. This is consistent with the experiment. Beyond the threshold value $I \approx 0.02$, the simulation results show that f_0 increases almost linearly with I, following a fitted function $f_0/f_{0,I=0} = 11.73I + 0.767$ (root mean square of residuals for fitting is 0.0423). To verify the universality of the linear increase of f_0 with I, parametric studies on the key parameters such as M and Re_H will be required, which is relegated to the future work. When I further increases, the experimental data become more dispersed, and non-monotonic behavior is observed.

3.3. Spatial growth rate

The inlet gas turbulence also has an impact on the spatial growth of the interfacial wave. As already qualitatively shown in Fig. 1, when turbulence is present at the gas inlet, the amplitude of the interfacial wave grows faster spatially. Due to the unsteady wave motion, the mean square of the liquid volume fraction fluctuations, $\overline{c'c'}$, is non-zero in a region near the interface, see Fig. 4. This region is referred to as the two-phase mixing layer since $0 < \bar{c} < 1$. The blues lines at the left boundary represent the separator plates. The thickness of the mixing layer, ξ, represents the amplitude of the interfacial wave. It can be observed from Fig. 4 that the layer thickness increases faster for $I = 0.071$ than that for $I = 0$ near the nozzle.

A quantitative measurement of ξ would require a threshold to determine the boundaries of the two-phase mixing layer. Here, we consider that a

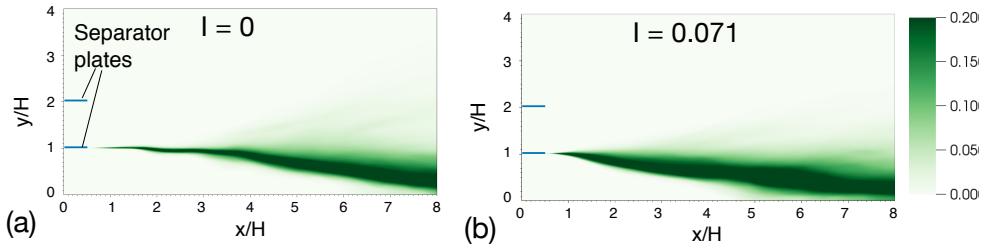

Figure 4: Mean square of liquid volume fraction fluctuations $\overline{c'c'}$ for (a) $I = 0$ and (b) $I = 0.071$. The two separator plates near the inlet are indicated by the blue lines.

spatial location is within the two-phase mixing layer if $\overline{c'c'} < 0.02$. The spatial growth of the ξ for different $I = 0$ and $I = 0.071$ are shown in Fig. 5(a). Both cases show an exponential growth of $\xi \sim \exp(\alpha_0 x)$ near the nozzle, where α_0 is the spatial growth rate along x. The threshold of $\overline{c'c'}$ for determining the mixing layer thickness will influence the value of ξ but not the growth rate α_0. The fluctuations in the mixing layer thickness for $I = 0.0$ are due to the finite averaging time and can be reduced by running the simulation for a longer time. Nevertheless, the present results are sufficient to measure the spatial growth rate.

Figure 5 clearly shows that when inlet gas turbulence is present, ξ increases spatially much faster. For $I = 0.071$, the spatial growth rate is $\alpha\delta_g \approx 0.473$, which is about 87% higher than that for $I = 0$. The variation of the spatial growth rate α_0 over I is shown in Fig. 5(b). Similar to the dominant frequency f_0, it is shown that α_0 changes little when I increases from 0 to 0.02. Yet, beyond the threshold value, $I = 0.02$, α_0 is observed to increase almost linearly with I, similar to f_0. The normalized spatial growth rate $\alpha_0/\alpha_{0,I=0}$ is well fitted by a linear function of $\alpha_0/\alpha_{0,I=0} \approx 15.60I + 0.719$ (with a root mean square of residuals as 0.0494).

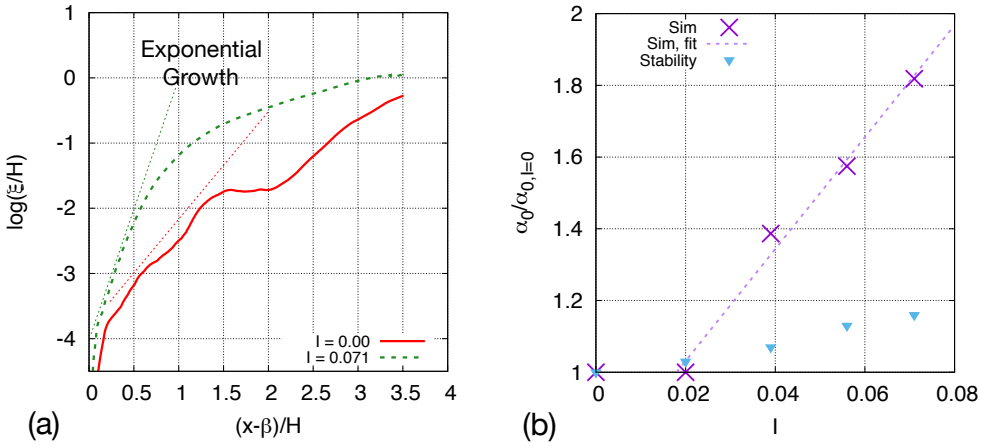

Figure 5: (a): Spatial growth of the mixing layer thickness ξ and (b) variation of the exponential growth rate α_0 as a function of the inlet gas turbulence intensity I.

As the mixing-layer thickness ξ continues to grow along the streamwise direction, the nonlinear effect and the influence from the bottom wall become important and the spatial growth rate decreases, see Fig. 5(a). The decrease in α_0 is faster for $I = 0.071$. As a result, ξ for $I = 0.071$ increases faster near the nozzle, but slower downstream, see Figs. 4 and 5(a). The difference between ξ for $I = 0$ and $I = 0.071$ first increases and then decreases (for $(x - \beta)/H \gtrsim 2$).

3.4. Linear stability analysis

For the case $I = 0$, linear viscous spatio-temporal stability analysis has been performed to identify the most unstable mode in a two-phase mixing layer [13, 16, 21, 18]. The perturbation is introduced on the streamfunction ψ, taking the form of normal modes: $\psi(x, y, t) = \phi(y) \exp[i(\alpha x - \omega t)]$, where α and ω are the complex wave number and frequency. Given a complex

frequency (ω_r, ω_i), the real and imaginary parts of the complex wave number (α_r, α_i) can be computed by solving the Orr-Sommerfeld equations. The details of the Orr-Sommerfeld equations and the solution methods have been explained in former works [13, 16, 18] and thus are not repeated here. If the branches for different ω_i "pinch", forming a saddle point on the $\alpha_r - \alpha_i$ plane (see Fig. 6(a)), then the instability is absolute. The saddle point represents the most unstable mode, yielding the dominant frequency (ω_r) and the spatial growth rate $(-\alpha_i)$ as shown in Fig. 6(b).

The most-unstable frequency and spatial growth rate predicted by linear viscous stability analysis are about $f_{0,stab}H/U_g = 0.06$ and $\alpha_{0,stab}\delta_g = 0.3$ for the case $I = 0$ [18], which are close to the simulation results $f_{0,sim}H/U_g \approx 0.05$ and $\alpha_{0,sim}\delta_g \approx 0.26$. The stability theory tends to overpredicts both the frequency and spatial growth rate for about 20%. Yet considering the complexity of the problem, the agreement is reasonable. Former studies have addressed the effect of confinement (finite stream thickness) on stability, but for the present case, it has been examined that the effect of confinement on the dominant frequency and the spatial growth rate is negligible.

Attempts have been made to incorporate the effect of gas inlet turbulence on the interfacial instability by using the eddy viscosity model [15, 21]. The sum of the molecular kinematic viscosity and the turbulent counterpart, namely $\nu_g^* = \nu_g + \nu_t$, is the effective gas viscosity, which is used as the gas viscosity in the stability analysis. Here, the eddy viscosity is calculated based on the shear Reynolds stress and the gradient of the mean velocity at the

interface and at the nozzle exit,

$$\nu_t \approx -\left.\frac{\widetilde{u''v''}|}{dU_g/dy}\right|_{y=H,x=\beta} = -\frac{\widetilde{u''v''}|_{y=H,x=\beta}}{U_g/\delta} \tag{8}$$

The values of the shear Reynolds stresses used here correspond to the maximum magnitudes of $\widetilde{u''v''}$ in the profiles shown in Fig. 2(c). The eddy and effective gas viscosities for different I considered in the present study are summarized in the table 3.

I	0	0.020	0.039	0.056	0.071
$\nu_t/(U_g\delta_g) = -\widetilde{u''v''}/U_g^2$	3.3×10^{-5}	0.0002	0.0008	0.00203	0.00355
$\nu_g^*/(U_g\delta_g)$	0.001	0.0012	0.0018	0.00303	0.00455
ν_g^*/ν_g	1	1.2	1.8	3.03	4.55
$f_{0,stab}/f_{0,I=0}$	1	1.03	1.07	1.13	1.16
$f_{0,sim}/f_{0,I=0}$	1	1	1.25	1.38	1.63
$\alpha_{0,stab}/\alpha_{0,I=0}$	1	1.01	1.07	1.14	1.17
$\alpha_{0,sim}/\alpha_{0,I=0}$	1	1	1.39	1.57	1.82

Table 3: Dominant frequency and spatial growth rates of the interfacial instability predicted by the linear stability analysis using eddy viscosity model, compare to the simulation results.

The stability analysis results showed that all cases considered are all absolutely unstable, characterized by the "pinching" of branches in the complex spatial wave number (α_r-α_i) plane, see Fig. 6(a). The frequency $f_{0,stab} = \omega_{r,0}/2\pi$ and spatial growth rate $\alpha_{0,stab} = -\alpha_{i,0}$ corresponding to the saddle points for all the cases considered are measured and summarized in table 3, compared with the simulation results. The theoretical and numerical results are also plotted in figures 3 and 5. Both the dominant frequency and the

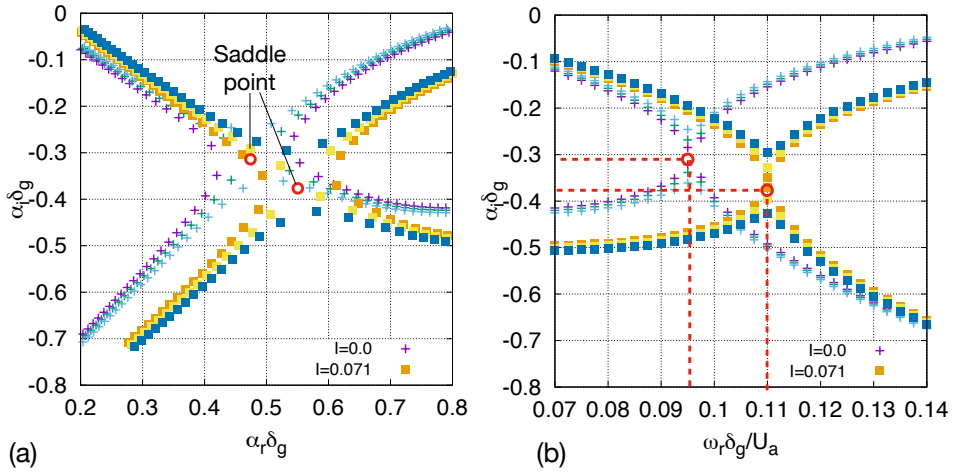

Figure 6: Spatial branches for different ω_i on (a) α_r-α_i and (b) ω_r-α_i planes. The symbols of plus signs and squares are for $I = 0$ and $I = 0.071$, respectively. Different colors denote different ω_i values. The red circles represent the saddle points. Here $U_a = \frac{U_g+U_l}{2}$ is used as the velocity scale.

spatial growth rate are found to increase with ν_t and I. Therefore, the overall trends that f_0 and α_0 increase with I were qualitatively captured by the model. However, the stability theory significantly underestimates the magnitudes for both of f_0 and α_0. This discrepancy between the stability theory with turbulent eddy-viscosity model has also been observed in the former work by Matas *et al.*[21].

The results seem to indicate that the Orr-Sommerfeld theory with a simple eddy-viscosity model is insufficient in predicting instability when inlet gas turbulence is present. A possible reason for the discrepancy is the significant anisotropic effect near the interface and the nozzle exit. The degree of anisotropy of turbulence can be measured by the second invariant, II_b, of

the normalized anisotropy tensor of Reynolds stresses, b_{ij} [29, 30], where

$$b_{ij} = \frac{\overline{u_i u_j}}{\overline{u_k u_k}} - \frac{1}{3}\delta_{ij} \tag{9}$$

and

$$\mathrm{II}_b = b_{ij} b_{ji} \,. \tag{10}$$

The results of II_b along with the boundaries of the two-phase mixing layer (indicated by the contour lines for $\overline{c'c'} = 0.02$) are shown in Fig. 7. It is known that II_b is positive definite and a large value indicates a high degree of anisotropy of turbulence. It is observed that II_b is substantial near the boundaries of the the two phase mixing layer. The anisotropy is induced by the background shear due to velocity difference between the gas and liquid streams. As the present Reynolds number is moderate, the large-scale anisotropy is transferred to the small scales [31] and the small-scale anisotropy influences the momentum transfer and the effective eddy viscosity. As a result, the isotropic eddy viscosity model used here may induce an error in the stability analysis and contribute to the discrepancy observed between the simulation results and model prediction. Further investigation to better incorporate the anisotropic effect of turbulence on the instability analysis, such as by employing an anisotropic eddy viscosity model [32], is required in our future work to improve the model prediction.

3.5. Turbulence development near the nozzle

As the interfacial instability plays a critical role in gas turbulence development near the interface, the influence of the inlet gas turbulence on the interfacial instability near the nozzle exit will also have an impact on the development of two-phase turbulence further downstream. The spatial

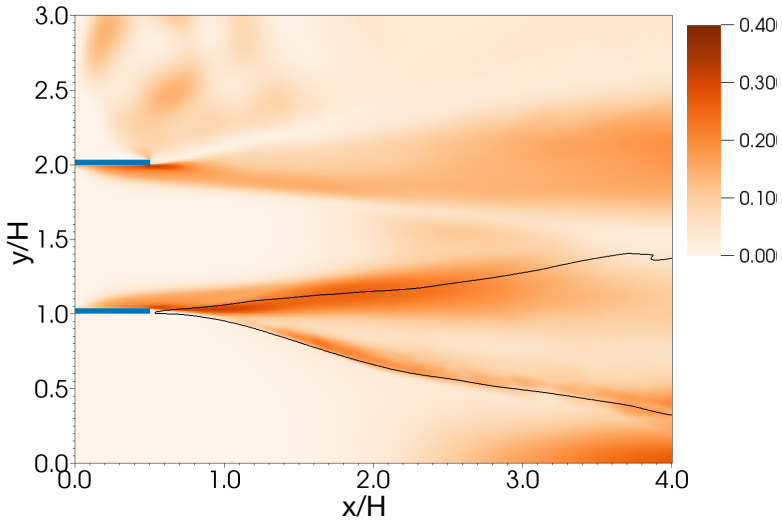

Figure 7: The second invariant, II_b, of the normalized anisotropy tensor of Reynolds stresses, b_{ij} near the nozzle exit. The boundaries of the two-phase mixing layer are indicated by black lines (the contour lines for $\overline{c'c'} = 0.02$).

development of the two-phase turbulence is investigated through turbulence statistics.

The time averaging starts at $t_0 \approx 200H/U_g$, when the mixing layer has reached a statistically stationary state, to about $t_1 \approx 460H/U_g$. This sampling time duration has been shown to be sufficient to obtain statistically converged results [18].

Due to the presence of two fluids of different densities, Favre averaging is used, which is defined as $\tilde{u} = \overline{\rho u}/\overline{\rho}$, and the fluctuation away from Favre-averaged quantity can be expressed as $u'' = u - \tilde{u}$. Then the averaged momentum equation can be expressed as

$$0 = -\frac{\partial \overline{\rho}\tilde{u}_i\tilde{u}_j}{\partial x_j} - \frac{\partial \overline{p}}{\partial x_i} + \frac{\partial}{\partial x_j}\overline{\left[\mu\left(\frac{\partial u_i}{\partial x_j} + \frac{\partial u_j}{\partial x_i}\right)\right]} + \overline{f_{s,i}} + \frac{\partial \tau_{ij}}{\partial x_j}, \qquad (11)$$

where τ_{ij} is the Reynolds stress tensor $\tau_{ij} = -\overline{\rho}\widetilde{u_i''u_j''}$.

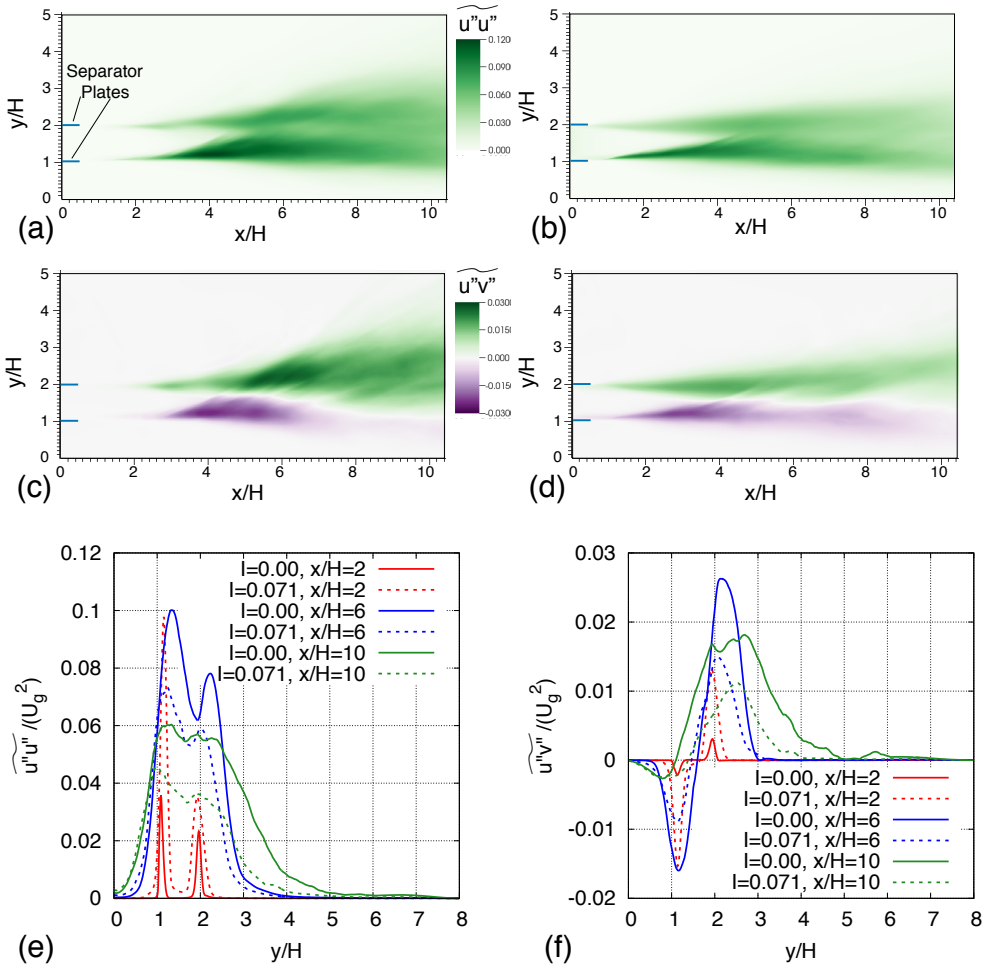

Figure 8: Spatial and temporal evolution of Reynold stresses, $\widetilde{u''u''}$ and $\widetilde{u''v''}$, for $I = 0$ and 0.071 in (a, c, e) and (b, d, f) respectively.

The distribution of normal and shear Reynolds stresses over mean density for $I = 0$ and 0.071 are shown in Fig. 8 (a)-(d). (Here $\widetilde{u''u''}$ and $\widetilde{u''v''}$ are simply referred to as Reynolds stresses, following the convention of turbulence research [29].) The profiles of $\widetilde{u''u''}$ and $\widetilde{u''v''}$ at different streamwise locations are shown in Fig. 8 (e)-(f). Since the values of I used in the present study are all quite small, the Reynolds stresses within the nozzle for the two cases are very similar. However, outside of the nozzle, the the difference between Reynolds stresses for $I = 0$ and 0.071 are significantly magnified.

Furthermore, the increases of Reynolds stresses along the streamwise direction is more rapid for $I = 0.071$. At $x/H = 2$, the normal Reynolds stress for $I = 0.071$ is almost three times as that for $I = 0$. The difference in shear stress is even larger, $-\widetilde{u''v''}/U_g^2$ for $I = 0$ and $I = 0.071$ at $x/H = 2$ are 0.002 and 0.015, respectively. This clearly shows that the turbulence development near the interface is appreciably enhanced when turbulent fluctuations are present at the gas inlet.

The development of the gas turbulence and the interfacial instability interact with each other. The addition of inlet gas turbulence makes the interaction even more complicated. On one hand, the inlet gas velocity fluctuations enhances the development of the gas turbulence near the interface. The enhanced gas turbulence near the interface in turn strengthens the momentum transfer between the gas and liquid streams, resulting in a faster growth of the interfacial stability. The increases of the dominant frequency and spatial growth rate over I are clear evidences of that. On the other hand, the higher frequency and growth rate of interfacial instability influence the interface deformation and the interfacial wave dynamics. Since the interfa-

cial waves behaves like "roughness" or obstacles to the gas stream, the faster growth of the interfacial waves will perturb the gas flow and in turn speed up the development of gas turbulence near the interface (or the transition to turbulence when the gas inlet is laminar). It is noted that, the stability analysis with the eddy viscosity model only considers the effect of turbulence on the interfacial stability, with the back effect of the modulated interfacial instability on the turbulence development ignored. This may be another potential reason for the discrepancy between the model prediction and the experimental and numerical results beyond the anisotropic effect discussed above.

3.6. Downstream turbulent two-phase mixing layer development

While the magnitudes of the Reynolds stresses near the nozzle increases with I, it is interesting to notice that the Reynolds stresses further downstream of the nozzle exit ($4 \lesssim x/H \lesssim 6$) for $I = 0.071$ are actually smaller than those for $I = 0$. In other words, the downstream two-phase mixing layer becomes "less" turbulent when turbulent fluctuations are added at the gas inlet. The spatial evolution of the Reynolds stresses profiles are shown in Figs. 8 (e) and (f). For $I = 0.071$ the magnitudes of Reynolds stresses near the interface decrease monotonically with x for $x/H > 2$. In contrast, for $I = 0$ the magnitudes of Reynolds stresses first increase and then decrease. The decay of Reynolds stresses near the interface over x for $I = 0.071$ is faster than that for $I = 0$. As a result, the Reynolds stresses magnitudes for $I = 0$ overtakes those for $I = 0.071$ at about $x/H = 4$, see Figs. 8 (a)–(d).

Since the development of gas turbulence near the interface is enhanced by the inlet gas turbulence, the rate of dissipation of turbulent kinetic energy,

ϵ, also increases. The TKE dissipation is computed as

$$\epsilon = -\overline{\mu\left(\frac{\partial u_i''}{\partial x_j} + \frac{\partial u_j''}{\partial x_i}\right)\frac{\partial u_i''}{\partial x_j}}\,, \tag{12}$$

and can be obtained by post-processing the DNS data. The results of ϵ for $I = 0$ and 0.071 are shown in Fig. 9, and it is obvious that the dissipation near the nozzle for $I = 0.071$ is much stronger than for $I = 0$, indicating a faster consumption of the turbulent kinetic energy, which in turn takes away kinetic energy from the mean flow. The mean stream-wise velocity for $I = 0$ and 0.071 are shown in Figs. 10(a) and (b), respectively. The mean velocity at the center of the gas stream is plotted in Fig. 10(c), from which it can be seen that $\overline{u}$ decreases faster along x for $I = 0.071$ than $I = 0$. As a result, the interaction between the gas and liquid streams downstream for $I = 0.071$ becomes weaker. In contrast, for $I = 0$ the gas stream does not become fully turbulent until $x/H > 4$, and much less kinetic energy is dissipated. Then the gas stream retains its momentum until it interacts with the interfacial wave downstream, resulting in a flow separation in the wake of the interfacial wave and a violent breakup of the liquid sheet. The liquid sheet fragmentations generate of large number of turbulent vortical structures (see Fig. 1(a)), which explains why the magnitudes of Reynolds stresses downstream at about $x/H \approx 4$ for $I = 0$ are larger than those for $I = 0.071$.

4. Conclusions

The destabilization of a planar liquid stream assisted by a laminar or turbulent gas stream has been studied through DNS. Particular attention is

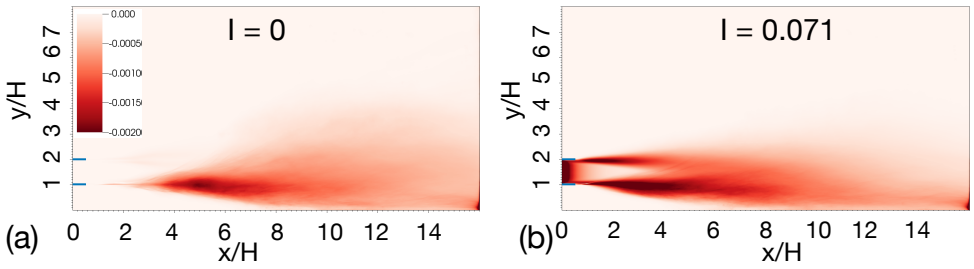

Figure 9: Rate of turbulent kinetic energy dissipation ϵ for (a) $I = 0$ and (b) $I = 0.071$.

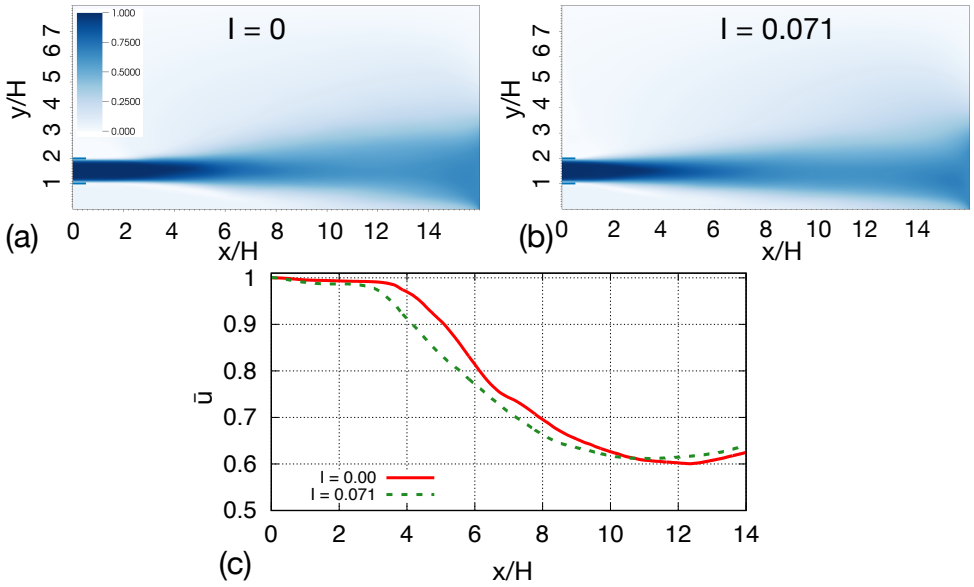

Figure 10: Mean streamwise velocity $\overline{u}$ for (a) $I = 0$ and (b) $I = 0.071$. (c) The decay of $\overline{u}$ at the center of the gas jet (y/H=1.5).

paid on the effect of the intensity of inlet gas turbulence, I, on the gas-liquid interfacial instability and the development of the two-phase turbulent mixing layer. The dominant frequency and the spatial growth rate of the interfacial waves are measured. It is found that both of them increase almost linearly with the inlet gas turbulence intensity, passed a threshold value. The results of dominant frequency obtained from DNS show a good agreement with the experimental data. A linear viscous spatial-temporal stability analysis is performed using the turbulent eddy viscosity model to mimic the effect on inlet gas turbulence. The simple model captures the increasing trends for the dominant frequency and the spatial growth rate over I. However, the modified stability model significantly under-predicts both the dominant frequency and the spatial growth rate. Furthermore, the modulated interfacial instability is shown to have a strong impact on the development of the gas turbulence near the interface. When turbulent fluctuations are added at the gas inlet, the Reynolds stresses near the nozzle exit are significantly magnified. As the turbulent kinetic energy dissipation is enhanced near the nozzle exit when the inlet gas turbulence is present, the mean streamwise velocity of the gas stream decreases along the streamwise direction faster. The interaction between the gas stream and the interfacial wave actually becomes weaker downstream, resulting in smaller magnitudes of the Reynolds stresses compared to those when the inlet gas stream is laminar. When the gas inflow is turbulent, interfacial waves develop faster and experience stronger interactions with the gas stream. As a result, interfacial waves break at locations closer to the nozzle compared to the case with a laminar gas inlet. Furthermore, the dominant mode of wave breakup and the size distribution of the

droplets formed also change when the gas inlet becomes turbulent. Further investigation of the effect of gas inlet turbulence on the spray characteristics will be relegated to our future work.

Acknowledgement

The present work is supported by the startup fund from Baylor University. YL is also partially supported by National Science Foundation (NSF #1853193). We thank Stephane Zaleski and Gretar Tryggvason and other developers of the solver *PARIS-Simulator*. The simulations were performed at the Texas Advanced Computing Center (TACC) at The University of Texas at Austin and also the Oak Ridge Leadership Computing Facility. The simulation data were post-processed at the Baylor cluster. The simulation data are visualized by the software VisIt developed by Lawrence Livermore National Laboratory.

References

[1] J. C. Lasheras, E. J. Hopfinger, Liquid jet instability and atomization in a coaxial gas stream, Annu. Rev. Fluid Mech. 32 (2000) 275–308.

[2] H. Helmholtz, On discontinuous movements of fluids, Philos. Mag. 36 (1868) 337–346.

[3] W. Thomson, Hydrokinetic solutions and observations, Philos. Mag. 42 (1871) 362.

[4] R. H. Rangel, W. A. Sirignano, Nonlinear growth of Kelvin–Helmholtz

instability: effect of surface tension and density ratio, Phys. Fluids 31 (1988) 1845–1855.

[5] E. Villermaux, Mixing and spray formation in coaxial jets, J. Propul. Power 14 (1998) 807–817.

[6] P. Marmottant, E. Villermaux, On spray formation, J. Fluid Mech. 498 (2004) 73–111.

[7] J.-P. Matas, S. Marty, A. Cartellier, Experimental and analytical study of the shear instability of a gas-liquid mixing layer, Phys. Fluids 23 (2011) 094112.

[8] Y. Renardy, Instability at the interface between two shearing fluids in a channel, Phys. Fluids 28 (1985) 3441–3443.

[9] A. P. Hooper, W. G. C. Boyd, Shear-flow instability due to a wall and a viscosity discontinuity at the interface, J. Fluid Mech. 179 (1987) 201–225.

[10] T. Boeck, S. Zaleski, Viscous versus inviscid instability of two-phase mixing layers with continuous velocity profile, Phys. Fluids 17 (2005) 032106.

[11] C.-S. Yih, Instability due to viscosity stratification, J. Fluid Mech. 27 (1967) 337–352.

[12] P. Valluri, L. O. Naraigh, H. Ding, P. D. M. Spelt, Linear and nonlinear spatio-temporal instability in laminar two-layer flows, J. Fluid Mech. 656 (2010) 458–480.

[13] T. Otto, M. Rossi, T. Boeck, Viscous instability of a sheared liquid-gas interface: Dependence on fluid properties and basic velocity profile, Phys. Fluids 25 (2013) 032103.

[14] J.-P. Matas, Inviscid versus viscous instability mechanism of an air–water mixing layer, J. Fluid Mech. 768 (2015) 375–387.

[15] L. O'Naraigh, P. D. M. Spelt, S. J. Shaw, Absolute linear instability in laminar and turbulent gas–liquid two-layer channel flow, J. Fluid Mech. 714 (2013) 58–94.

[16] D. Fuster, J. P. Matas, S. Marty, S. Popinet, H. J., A. Cartellier, S. Zaleski, Instability regimes in the primary breakup region of planar coflowing sheets, J. Fluid Mech 736 (2013) 150–176.

[17] G. Agbaglah, R. Chiodi, O. Desjardins, Numerical simulation of the initial destabilization of an air-blasted liquid layer, J. Fluid Mech. 812 (2017) 1024–1038.

[18] Y. Ling, D. Fuster, G. Tryggvasson, S. Zaleski, A two-phase mixing layer between parallel gas and liquid streams: multiphase turbulence statistics and influence of interfacial instability, J. Fluid Mech. 859 (2019) 268–307.

[19] Y. Ling, D. Fuster, S. Zaleski, G. Tryggvason, Spray formation in a quasiplanar gas-liquid mixing layer at moderate density ratios: A numerical closeup, Phys. Rev. Fluids 2 (2017) 014005.

[20] M. Klein, A. Sadiki, J. Janicka, A digital filter based generation of inflow

data for spatially developing direct numerical or large eddy simulations, J. Comput. Phys. 186 (2003) 652–665.

[21] J.-P. Matas, S. Marty, M. S. Dem, A. Cartellier, Influence of gas turbulence on the instability of an air-water mixing layer, Phys. Rev. Lett. 115 (2015) 074501.

[22] A. Zandian, W. A. Sirignano, F. Hussain, Planar liquid jet: Early deformation and atomization cascades, Phys. Fluids 29 (2017) 062109.

[23] A. Zandian, W. A. Sirignano, F. Hussain, Understanding liquid-jet atomization cascades via vortex dynamics, J. Fluid Mech. 843 (2018) 293–354.

[24] D. Fuster, T. Arrufat, M. Crialesi-Esposito, Y. Ling, L. Malan, S. Pal, R. Scardovelli, G. Tryggvason, S. Zaleski, A momentum-conserving, consistent, volume-of-fluid method for incompressible flow on staggered grids, under review (2019).

[25] S. Popinet, An accurate adaptive solver for surface-tension-driven interfacial flows, J. Comput. Phys. 228 (16) (2009) 5838–5866.

[26] F. J. Salvador, S. Ruiz, M. Crialesi-Esposito, I. Blanquer, Analysis on the effects of turbulent inflow conditions on spray primary atomization in the near-field by direct numerical simulation, Int. J. Multiphase Flow 102 (2018) 49–63.

[27] J. Westerweel, C. Fukushima, J. M. Pedersen, J. C. R. Hunt, Mechanics of the turbulent-nonturbulent interface of a jet, Phys. Rev. Lett. 95 (2005) 174501.

[28] P. E. Dimotakis, Two-dimensional shear-layer entrainment, AIAA J. 24 (1986) 1791–1796.

[29] S. B. Pope, Turbulent flows, Cambridge Univ Press, 2000.

[30] J. L. Lumley, G. R. Newman, The return to isotropy of homogeneous turbulence, J. Fluid Mech. 82 (1977) 161–178.

[31] P. K. Yeung, J. G. Brasseur, The response of isotropic turbulence to isotropic and anisotropic forcing at the large scales, Phys. Fluids A 3 (1991) 884–897.

[32] D. Carati, W. Cabot, Anisotropic eddy viscosity mode, in: Proc. Summer Program of Center of Turbulence Research, 1996, pp. 249–258.